Measurement of residues from the ^{6}Li +Zn reaction: Analysis of fusion phenomena below 7.1 MeV/nucleon

Ankur Singh [1], Moumita Maiti [1,*], T. N. Nag,[2] and S. Sodaye[2]
[1]*Department of Physics, Indian Institute of Technology Roorkee, Roorkee 247667, Uttarakhand, India*
[2]*Radiochemistry Division, Bhabha Atomic Research Centre, Mumbai 400085, India*

(Received 14 March 2023; revised 13 July 2023; accepted 31 July 2023; published 21 August 2023)

We report the measurement of fusion-evaporation residues emerging from ^{6}Li +Zn reaction within the 21–43 MeV energy range in conjunction with the underlying reaction dynamics in the scarcely explored light-medium mass region. The stack foil activation technique followed by offline γ spectroscopy was employed to measure the cross sections of residues populated in the reaction. The measured data were compared with theoretical predictions from statistical model codes like PACE4 and EMPIRE3.2.2 to probe the underlying reaction dynamics. The imitation of *n*- and *p*-channel data grossly by both the model codes suggests the production of residues via the complete fusion (CF) mode, while the enhancement observation in α-channel cross sections hints at the signatures of breakup fusion in addition to the dominant CF. We report a new branching intensity of 93.31 keV γ-line retrieved experimentally from ^{67}Ga decay following the end of bombardment activity in each target foil. The optimized production of ^{67}Ga is also reported from the application perspective.

DOI: 10.1103/PhysRevC.108.024607

I. INTRODUCTION

The cluster structure of weakly bound particles (WBPs) has boosted nuclear research for over a decade [1]. Scientists have scrutinized the multifarious reaction mechanisms, such as complete fusion (CF), incomplete fusion (ICF), preequilibrium emission (PEQ), fusion-fission, quasifission, transfer, etc., in heavy-ion (HI) reactions with strongly and weakly bound particles. CF processes are anticipated in central collisions, implied by a complete transfer of angular momentum from projectile to target within $0 < \ell \leqslant \ell_{\rm crit}$, in contrast to the peripheral processes (ICF) occurring at $\ell \geqslant \ell_{\rm crit}$ due to partial angular momentum transfer. However, the potential pocket vanishes for the latter case, restricting the fusion from occurring until a viable angular momentum is released through breakup [2]. Besides CF-ICF, other processes like sequential complete fusion and elastic breakup have also been exhibited by WBPs. However, the compound nucleus (CN) formed through direct CF or sequential CF remains indistinguishable. The evaporation of light particles such as *n* or *p* from the hot composite system prior to attaining equilibrium is termed the PEQ process. PEQ has been extensively studied in *n*-emitting channels, seen in the high energy tail of the excitation function [3].

In literature, ^{6}Li breakup has been manifested as a consequence of direct prompt breakup from continuum nonresonant states, sequential breakup into $\alpha + d$ fragments from resonance states (1^{+}, 2^{+}, 3^{+}) and/or the transfer-triggered breakups into $\alpha + p$ and $\alpha + \alpha$ through *n* stripping and *d* pickup, respectively [4–6]. Luong *et al.* [4] and Santra *et al.* [5] suggested the dominance of transfer-triggered breakup over a direct breakup ($\alpha + d$), contrary to Chattopadhyay *et al.* [7]. However, *d* capture contributing to large α production dominates the other processes, as stated by Santra *et al.* [8]. The disentanglement of direct breakup and transfer-triggered breakup poses experimental challenges due to the same resulting fusion products, especially in inclusive measurements. Compared to the one-dimensional barrier penetration model (1D-BPM) predictions, CF suppression has been attended in several studies with WBP at above-barrier energies [9–11]. The role of repulsive polarization potential due to breakup couplings in the continuum, enhancing the fusion barrier height and thus depleting the CF channel flux, has been understood to explain suppression. In this series, Kumawat *et al.* [9] and Hu *et al.* [10] report ≈15–30% suppression in light-medium mass nuclei, while ≈30–40% suppression has been reported in heavy systems [11]. Furthermore, CF suppression independence of target charge (Z_T) was reported by Kumawat *et al.* [9] and Gasques *et al.* [12], contrary to the increasing trend suggested by Rath *et al.* [13]. The enhancement below the barrier has been contemplated as the effect of transfer channels and inelastic couplings [13,14]. In contrast, hindrance has been reported in the deep sub-barrier region.

Dynamics of low energy (3–10 MeV/nucleon) reaction has been investigated over the years using activation technique, particle-γ coincidence, and recoil range distribution measurements with α-clustered beams. The effect of several entrance channel parameters such as bombarding energy, projectile structure (Q_α value), mass asymmetry (μ), Z_T, deformation (β), etc., on reaction dynamics in the case of clustered particles has been explored [15–19]. At a constant relative velocity, more breakup for relatively loosely bound projectiles over others and larger mass asymmetry have been observed

*Corresponding author: moumita.maiti@ph.iitr.ac.in

[15,16]. Moreover, Trautmann *et al.* [20] discussed the peripheral nature of ICF. A review by Gerschel *et al.* [21] elaborates on the localization of driving angular momentum window dependency on target deformation. However, recent studies [16,22] suggest the fusion of ℓ boundaries depicting breakup fusion occurrence below $\ell_{\rm crit}$, contrary to the sharp cutoff approximation in the sum-rule model [23]. We report a new set of measured residual cross sections from the ^{6}Li + $^{\rm nat}$Zn reaction alongside the role of underlying mechanisms in the light-medium mass region. Besides reaction dynamics, WBP reactions help to optimize the production of radionuclides that have found applications in nuclear medicine, as is the case in our study. Several diagnostic or therapeutic purposes are being met through consistent efforts from researchers working in this field [24]. Thus, precisely measured decay data must be ensured, though we report a discrepancy in the intensity value of 93.31 keV γ line from the decay of application-based ^{67}Ga reported in databases in this regard. Ambiguous findings in the literature entail a comprehensive measurement of data employing distinct techniques and investigation of reaction dynamics and entrance channel dependencies at near-barrier energies to draw better conclusions, especially in the context of WBPs in the scarcely explored medium mass region.

For the first time, we report the residual cross section measurement in the ^{6}Li reaction on a $^{\rm nat}$Zn target within the 21–43 MeV energy domain and analysis of associated fusion phenomena. The experimental methodology and theoretical model calculations are discussed in Secs. II and III, respectively. Section IV discusses the experimental findings, and Sec. V concludes the report.

II. EXPERIMENTAL DETAILS

The experiment was performed using a low energy (3.5–7.1 MeV/nucleon) beam of ^{6}Li^{+3} ions delivered by the pelletron facility at BARC-TIFR, Mumbai, India. Self-supported thin $^{\rm nat}$Zn foils (99.99% pure) of thickness 2.8 mg/cm^2 and Al backing having thickness 1.8 mg/cm^2 were assembled to fabricate the target matrix after rolling. An Al foil was planted between two successive target foils to suffice the purpose of energy degrader and residue catcher. Target matrices were irradiated with varying energy to ensure a slight overlap of energies between successive irradiations. Monte Carlo simulation-based stopping and range of ions in matter (SRIM) code [25] was used to compute the energy degradation through the target and catcher foil. The energy at the center of a foil was obtained by averaging the entrance and exit energies. The irradiation time was decisively estimated according to the half-lives of the radionuclides expected in the reaction. The beam current was measured to be almost constant during the experiment; the beam was dumped into the electron-suppressed Faraday cup positioned at the rear of the target-catcher assembly. The average beam flux and irradiation dose were measured to be $\approx 5.6 \times 10^{10}$ particles/s and $\approx$391 μC, respectively.

After the irradiation, the off-beam measurements were done using a precalibrated high-purity germanium (HPGe) detector having energy resolution $\leqslant$ 2.0 keV at the 1332 keV energy γ ray of ^{60}Co to assess the induced residual activity. The γ spectra were recorded using a multichannel analyzer coupled to a PC operating with GENIE-2K (Canberra) software. The calibration of the detector was performed for energy and efficiency using the standard sources ^{152}Eu (13.506 yr), ^{137}Cs (30.08 yr), and ^{60}Co (5.27 yr) of known strengths. Subsequently, the γ-spectrum analysis was performed to identify the residues populated in the reaction from their characteristic γ rays and decay profiles. Dead time corrected and background subtracted photopeak counts were considered to determine the residual production cross sections at each bombarding energy using the well-known activation formula [26,27]. The nuclear spectroscopic data used in evaluating residual cross sections are tabulated in Table I. The measured data have an associated average uncertainty of ≈12–14%, contributed by the following sources: (i) Uncertainty in the target thickness measurement was ≈2%. (ii) Inaccuracy in detection efficiency was $\leqslant$ 2%. (iii) The beam current fluctuations resulted in ≈5–7% of uncertainty in the beam flux. (iv) There was statistical uncertainty in the photopeak counts. Finally, (v) the energy degradation at successive target-catcher foils contributed to the uncertainty in beam energy, which in turn has contributions from uncertainty in target thickness and SRIM calculation.

III. THEORETICAL MODEL CALCULATIONS

To decipher the underlying reaction mechanisms, we employed statistical model calculations using PACE4 [28] and EMPIRE3.2.2 [29] codes. A brief description of the two codes is given here with the set of input parameters used in the calculations

PACE4. Preinstalled in the LISE++ program, PACE4 is a Monte Carlo simulation based statistical code that predicts the residual cross sections in the framework of CF dynamics comprising equilibrium (EQ) processes. The Hauser-Feshbach (HF) formalism [30] was deployed to follow the decay sequence of an excited CN, where angular momentum coupling is preserved at each deexcitation stage. A Monte Carlo method with large deexcitation cascades (100 000 in the present case) governs the correlation between emitted particles, γ rays, energy, and angular distribution. The Bass model [31] estimates the HI fusion cross section and initial spin distribution. Transmission coefficients for the evaporation of light particles were estimated from the optical model. The approach of Hill and Wheeler [32] ensures the quantum mechanically treated transmission probabilities. Level density (LD) computed using the Gilbert-Cameron formalism was considered with a variable LD parameter $a = A/K$, where A is the mass number of the CN and K is a free parameter varied to obtain the best fit to the experimental data. $K = 10$ was used in the present analysis, although the sensitivity of theoretical cross sections was also checked with $K = 8$ and 9. The ARATIO parameter defined as a_f/a_n and the yrast parameter were set to unity in the present calculations, where a_f and a_n are the LD parameters for fission and neutron evaporation, respectively. PACE4 does not account for the direct and PEQ processes.

EMPIRE3.2.2. This is a versatile nuclear reaction code that accounts for the reaction mechanisms such as EQ, PEQ, and

TABLE I. Nuclear spectroscopic data [33] of residues populated in the ^{6}Li +^{nat}Zn reaction.

Nuclide	J^{π}	$T_{1/2}$	Decay mode (%)	E_{γ} (keV) [I_{γ} (%)]
^{72}As	2^{-}	26 h	ϵ[a] + β^{+}(100)	629.92 [8.07], 833.99 [81]
^{71}As	$5/2^{-}$	65.3 h	$\epsilon + \beta^{+}$(100)	174.954 [82.4], 326.785 [3.05] 499.876 [3.64], 1095.49 [4.1]
^{70}As	4^{+}	52.6 min	$\epsilon + \beta^{+}$(100)	252.46 [2.71], 595.11 [18.8] 607.34 [4.3], 668.21 [22.1] 743.62 [22.1], 905.61 [11.2] 1113.6 [20.6], 1338.76 [9] 1411.86 [8.7], 1522.55 [4.3] 1707.61 [17.5], 2019.16 [16.6]
^{69}As	$5/2^{-}$	15.2 min	$\epsilon + \beta^{+}$(100)	145.96 [4.94], 232.73 [10.9]
^{69}Ge	$5/2^{-}$	39.05 h	$\epsilon + \beta^{+}$(100)	318.63 [1.55], 574.11 [13.3] 871.98 [11.9], 1106.77 [36]
^{67}Ge	$1/2^{-}$	18.9 min	$\epsilon + \beta^{+}$(100)	167.01 [84], 828.3 [3] 911.2 [3.1], 914.8 [3] 1472.8 [4.9], 1809.4 [1.32]
^{66}Ge	0^{+}	2.26 h	$\epsilon + \beta^{+}$(100)	108.85 [10.6], 190.2 [5.7] 245.71 [5.43], 272.97 [10.6] 338.05 [8.8], 381.85 [28.3] 470.62 [7.5], 536.74 [6.2] 705.94 [4.3]
^{68}Ga	1^{+}	67.71 min	$\epsilon + \beta^{+}$(100)	1077.34 [3.22]
^{67}Ga	$3/2^{-}$	3.2617 d	$\epsilon + \beta^{+}$(100)	93.31 [38.81], 184.576 [21.41] 208.95 [2.46], 300.217 [16.64] 393.527 [4.56]
^{66}Ga	0^{+}	9.49 h	$\epsilon + \beta^{+}$(100)	1039.22 [37], 1918.329 [1.99] 2189.616 [5.3], 2422.525 [1.88]
^{65}Ga	$3/2^{-}$	15.2 min	$\epsilon + \beta^{+}$(100)	115.09 [54], 153 [8.9] 751.8 [8.1]
^{71m}Zn	$9/2^{+}$	3.96 h	β^{-}(100)	386.28 [91.4], 487.34 [61.2] 620.19 [55.8]
^{69m}Zn	$9/2^{+}$	13.756 h	IT[b](99.97), β^{-}(0.03)	438.634 [94.85]
^{65}Zn	$5/2^{-}$	243.93 d	$\epsilon + \beta^{+}$(100)	1115.539 [50.04]
^{63}Zn	$3/2^{-}$	38.47 min	$\epsilon + \beta^{+}$(100)	962.06 [6.5]
^{61}Cu	$3/2^{-}$	3.339 h	$\epsilon + \beta^{+}$(100)	282.956 [12.7], 373.05 [2.14] 656.008 [10.4], 1185.234 [3.6]

[a]Electron capture.
[b]Isomeric transition.

direct reactions emerging from a HI interaction over a wide range of energies and projectiles. The code has adopted the full-featured HF model with width fluctuation correction to study the EQ process. Quantum mechanical models such as multistep compound (MSC) or multistep direct (MSD) and phenomenological models such as the exciton model (EM) with the Iwamoto-Harada cluster emission model or hybrid Monte Carlo simulation (HMS) are considered for the PEQ process in the framework of EMPIRE code. Due to poor understanding, MSC and MSD options are not widely employed. The direct reaction contribution is estimated using the coupled-channels approach for deformed nuclei and the distorted-wave Born approximation (DWBA) for slightly deformed/spherical nuclei. A simplified coupled-channels calculation (CCFUS) which considers inelastic excitations and transfer channels independently was used to estimate the HI fusion cross section. The optical model computes the transmission coefficients for particle evaporation. The code reads the inputs such as nuclear masses, level densities, ground state deformations, discrete levels, decay schemes, optical model parameters, γ-ray strength functions, and fission barrier internally from RIPL-3 library [34]. In the present analysis, we used the HF model with default width fluctuation correction and EM with mean free path parameter PCROSS = 0.5 to fit the measured cross sections. Three options are available for the phenomenological level density models, viz., the Gilbert-Cameron model (GC) [35], the generalized superfluid model (GSM) [36], and the enhanced generalized superfluid model (EGSM) [37] were used to test the sensitivity of theoretical calculations. These models incorporate the collective excitation (rotational/vibrational) effects on level density and use the Ignatyuk energy-dependent level density parameter, which follows the shell effect dependency on excitation energy. EGSM treats the angular momentum more legitimately among all the three level density models, which is quite favorable for HI fusion reactions.

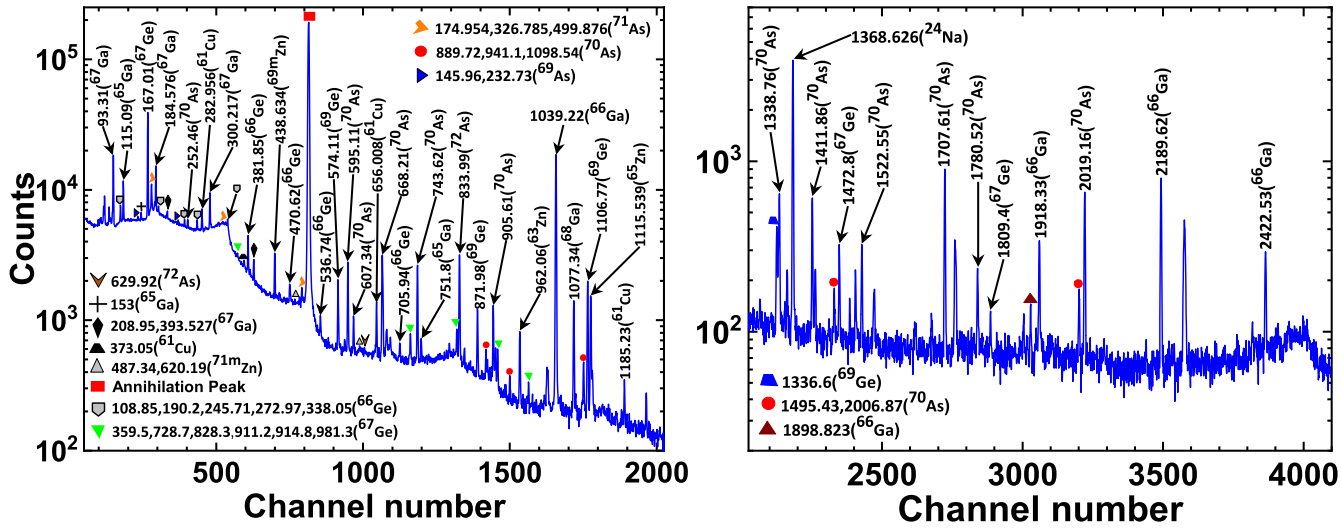

FIG. 1. Typical γ-ray spectrum of 43 MeV ^{6}Li irradiated Zn foil, collected 46 min after the end of bombardment (EOB). The γ peaks of residues are marked with energies in keV.

IV. RESULTS AND DISCUSSION

A comprehensive analysis of the time-resolved γ-ray spectrum ensured the production of 16 radionuclides, ^{72,71,70,69}As, ^{69,67,66}Ge, ^{68,67,66,65}Ga, ^{71m,69m,65,63}Zn, and ^{61}Cu, in ^{6}Li fusion with a Zn target within 21–43 MeV energy range. A typical γ-ray spectrum collected 46 minutes after the end of bombardment (EOB) is portrayed in Fig. 1. Residues populated in the target matrix were identified through their characteristic γ rays and half-lives. Table II tabulates the measured residual cross sections. The following subsection discusses the revised experimental branching intensity of the 93.31 keV γ line from ^{67}Ga decay. The experimental excitation functions (EFs) of residues compared to theoretical estimates from PACE4 and EMPIRE3.2.2 are displayed in Figs. 3–6. Since $^{\text{nat}}$Zn has a contribution from five abundant isotopes, viz., ^{64}Zn (49.17%), ^{66}Zn (27.73%), ^{67}Zn (4.04%), ^{68}Zn (18.45%), and ^{70}Zn (0.61%), the reported theoretical estimates also assume weighted contributions from these isotopes (in accord with the abundance-wise contribution in experimental data [26,38–40]). The measured data are symbolized in EF plots with associated uncertainties, while curves denote the theoretical predictions.

A. Determination of 93.31 keV γ-line intensity from ^{67}Ga decay

Tracking the EOB activity (A_{EOB}) of ^{67}Ga residue in the target matrix, we observed the measured activity for the 93.31 keV γ-line being almost half the values calculated from other lines despite having the same measured half-lives [Fig. 2(a)]. This discrepancy is speculated to result from uncertainty prevailing in the reported intensity value in different databases [33,41–44], ranging from 38.81% to 39.2%. Obeying the formalism available in the literature [26,45,46], we estimated a new value of intensity for the 93.31 keV γ line in comparison with other lines [184.576 (21.41%), 208.95 (2.46%), 300.217 (16.64%), and 393.527 (4.56%)] of ^{67}Ga residue. Eleven target foils were used, and multiple activity measurements were recorded for each activated target foil with elapsed time to follow the decay profile of the residue. Each target foil furnished around 24 values of intensity (six values of intensity for the 93.31 keV γ line compared to each other γ line, and one value corresponding to each activity measurement). Thus, 264 closest data extracted from 11 foils were averaged to obtain the mean value reported in Fig. 2(b). The estimated overall mean intensity value comes out to be $21.65 \pm 0.23\%$, in close consonance with the value reported in Refs. [26,46]. The reported new value of intensity is further backed by the reproduced $A_{\text{EOB}} = 30475.0 \pm 277.8$ Bq (using the new value), which stands in the range deduced from other lines [Fig. 2(a)]. Table III displays the experimental intensity for the 93.31 keV γ line and half-life of ^{67}Ga residue compared to the values reported in databases and literature [26,46]. Caution should be used considering the reported discrepancy in the intensity value, and a dedicated experiment should be planned in this direction to address the ambiguity.

Note that, during the analysis, it was ensured that the production of ^{67}Ga in the present case is free of speculated contamination from ^{67}Cu, as the two radionuclides decay to the same daughter nucleus (^{67}Zn) resulting in almost identical energies of γ emissions. However, there is a drastic difference in the branching intensities of 184.576, 300.217, and 393.527 keV γ lines from these two radionuclides. This feature (suggested in literature [47,48]) was utilized to confidently judge the contamination-free production of ^{67}Ga as realized in our previous measurements for nearby systems [26,46,49]. Moreover, the consistent experimental cross sections (or A_{EOB}) obtained for all the γ peaks in all the target foils (except the 93.31 keV peak owing to the discrepancy in intensity value) utilizing the properties of ^{67}Ga rather than ^{67}Cu, experimental half-life from all γ-peaks in each target foil being in close consonance with that of ^{67}Ga, the consistent trend (without any deviation) of the measured EF of ^{67}Ga with the theoretical one [Fig. 5(b)], and energetically forbidden or negligible production (<0.05 mb at highest energy) of ^{67}Cu in ^{6}Li + $^{\text{nat}}$Zn

TABLE II. Experimental production cross sections of residues at various incident energies.

	Cross section (mb)							
E_{Lab} (MeV)	^{72}As	^{71}As	^{70}As	^{69}As	^{69}Ge$^{\mathrm{cum}}$	^{67}Ge	^{66}Ge	^{68}Ga
21.3±0.9	34.9 ± 4.1	21.9 ± 3.1	22.4 ± 3.2		18.5 ± 2.9	1.3 ± 0.2		26.1 ± 3.6
23.8±0.9	32.6 ± 3.8	40.1 ± 5.4	22.9 ± 2.9		48.4 ± 6.7	5.9 ± 0.7		35.2 ± 4.6
26.2±0.8	20.5 ± 2.4	52.6 ± 6.7	18.5 ± 2.7		76.0 ± 9.7	11.9 ± 1.3		36.6 ± 4.7
28.4±0.8	16.1 ± 2.1	65.4 ± 8.2	15.0 ± 2.1	7.3 ± 2.1	108.4 ± 13.1	21.8 ± 2.9	0.2 ± 0.1	40.7 ± 5.1
30.5±0.8	12.7 ± 1.6	69.6 ± 9.0	11.6 ± 1.6	7.5 ± 2.0	131.8 ± 15.6	29.7 ± 4.4	0.3 ± 0.1	42.4 ± 5.2
32.5±0.7	9.3 ± 1.3	65.3 ± 7.9	10.1 ± 1.6	8.8 ± 1.9	136.2 ± 17.2	33.1 ± 4.8	0.5 ± 0.2	43.1 ± 5.4
35.7±0.7	5.4 ± 1.0	58.6 ± 6.7	11.3 ± 1.6	17.2 ± 7.0	139.1 ± 15.3	69.8 ± 9.5	1.1 ± 0.2	56.2 ± 6.9
37.5±0.7	5.1 ± 0.9	51.9 ± 6.2	12.1 ± 1.7	18.2 ± 7.1	140.3 ± 16.0	71.1 ± 11.4	1.8 ± 0.4	58.8 ± 7.6
39.2±0.7	4.7 ± 0.8	41.1 ± 4.9	12.7 ± 1.8	16.7 ± 4.7	124.3 ± 14.2	63.2 ± 9.9	2.8 ± 0.6	65.8 ± 8.3
40.9±0.7	4.1 ± 0.8	34.2 ± 4.2	13.5 ± 1.9	15.7 ± 4.3	116.1 ± 12.6	59.6 ± 8.6	4.1 ± 0.7	71.5 ± 8.9
42.6±0.7	3.6 ± 0.7	24.6 ± 2.9	14.4 ± 1.9	10.6 ± 3.5	90.1 ± 10.5	43.9 ± 7.3	4.9 ± 0.9	70.6 ± 8.6
	Cross section (mb)							
E_{Lab} (MeV)	^{67}Ga$^{\mathrm{cum}}$	^{66}Ga$^{\mathrm{cum}}$	^{65}Ga	^{71m}Zn	^{69m}Zn	^{65}Zn$^{\mathrm{cum}}$	^{63}Zn	^{61}Cu
21.3±0.9	100.3 ± 13.3	1.2 ± 0.2	13.6 ± 2.4	0.10 ± 0.04	5.2 ± 0.6	198.7 ± 41.9		
23.8±0.9	169.9 ± 20.7	2.5 ± 0.5	15.0 ± 2.3	0.12 ± 0.05	5.8 ± 0.7	234.5 ± 47.3		0.4 ± 0.2
26.2±0.8	220.2 ± 26.1	5.7 ± 1.1	14.1 ± 2.3	0.12 ± 0.04	5.6 ± 0.6	286.7 ± 54.0		0.8 ± 0.3
28.4±0.8	295.7 ± 32.3	12.7 ± 2.1	13.9 ± 1.9	0.13 ± 0.04	6.1 ± 0.7	324.7 ± 59.8	1.8 ± 0.5	1.4 ± 0.4
30.5±0.8	352.1 ± 36.8	23.1 ± 3.7	12.2 ± 1.8	0.14 ± 0.05	6.2 ± 0.7	326.2 ± 61.6	2.7 ± 0.7	3.1 ± 0.6
32.5±0.7	364.2 ± 40.0	33.7 ± 4.8	10.4 ± 1.5	0.12 ± 0.04	5.7 ± 0.7	360.2 ± 64.6	3.1 ± 0.7	5.1 ± 0.9
35.7±0.7	370.2 ± 38.8	57.6 ± 6.9	23.0 ± 3.7	0.13 ± 0.04	5.8 ± 0.7	220.4 ± 36.0	6.0 ± 1.2	7.6 ± 1.3
37.5±0.7	370.3 ± 38.5	75.5 ± 9.7	21.6 ± 3.6	0.12 ± 0.04	5.9 ± 0.7	213.8 ± 28.2	8.7 ± 1.7	9.7 ± 1.4
39.2±0.7	338.9 ± 37.0	93.6 ± 12.9	18.8 ± 3.0	0.13 ± 0.04	5.6 ± 0.6	203.7 ± 35.6	14.1 ± 2.6	10.3 ± 1.5
40.9±0.7	320.4 ± 35.2	120.2 ± 15.8	16.7 ± 2.4	0.13 ± 0.04	5.7 ± 0.6	218.4 ± 30.1	21.1 ± 3.0	11.8 ± 1.6
42.6±0.7	253.8 ± 28.4	128.7 ± 15.3	16.1 ± 2.7	0.12 ± 0.05	4.8 ± 0.6	196.9 ± 32.2	22.8 ± 3.1	11.3 ± 1.6

suggested by both the theoretical calculations firmly validate our conclusion.

B. Analysis of excitation functions

xn channel. Evaporation of neutrons from the CN experimentally yields four residues, ^{72,71,70,69}As, in the ^{6}Li reaction on Zn. Measured EFs of these residues compared with theoretical estimations from PACE4 ($K = 10$) and EMPIRE with EGSM, GSM, and GC level densities are displayed in Fig. 3. Figure 3(a) depicts that EMPIRE with EGSM well reproduces the measured data for ^{72}As, compared to GSM and GC calculations. GSM and GC also describe the data within uncertainties in the low energy region up to 32.5 MeV and overestimate above it, whereas PACE4 satisfies the data well within uncertainties above 30.5 MeV and overestimates below this energy. As suggested by theory, ^{72}As may dominantly emerge via $2n$ and $4n$ channels in ^{6}Li fusion with ^{68}Zn and ^{70}Zn isotopes of $^{\mathrm{nat}}$Zn, respectively, with ^{68}Zn contributing effectively in the low energy region and an almost similar contribution from ^{68,70}Zn at higher energies, with an insignificant contribution from ^{66}Zn (γ channel) and ^{67}Zn ($1n$ channel) isotopes. EMPIRE with EGSM and PACE4 both comply with the experimental data of ^{71}As within the studied energy range, as shown in Fig. 3(b), while GSM and GC explain the data in a higher energy window of 35.7–42.6 MeV only and deviate from the low energy data. Figure 3(c) demonstrates the abundance-wise contribution from constituent isotopes of Zn in the population of ^{71}As residue theoretically to justify the trend of measured EF, where the solid and dotted curves represent the EMPIRE (EGSM) and PACE ($K = 10$) calculations, respectively. One may notice that at lower energies the contribution comes from ^{6}Li fusion with ^{66,67,68}Zn isotopes, while at higher energies ^{66,67,68,70}Zn isotopes (or $1n$, $2n$, $3n$, and $5n$ channels, respectively) contribute with predominating yield from ^{68}Zn throughout the energy range. Thus, we observe an unusually broad Gaussian effective excitation function (black color) owing to the contribution from constituting isotopes of Zn in line with the thoroughly reproduced trend of measured EF. Figure 3(d) compares the measured EF of ^{70}As residue with theoretical ones, which may be populated via γ, $2n$, $3n$, and $4n$ channels in ^{6}Li reactions on ^{64}Zn, ^{66}Zn, ^{67}Zn, and ^{68}Zn isotopes, respectively, subject to the respective reaction thresholds, with ^{66}Zn majorly contributing at lower energies, ^{68}Zn at higher energies, and ^{67}Zn at intermediate energies. Thus, the experimentally observed valley-shaped effective EF can be justified in consonance with the theoretical one. EMPIRE with EGSM matches the data within experimental errors at higher energies with an overestimation below 35.7 MeV. GSM matches the data within uncertainties up to 37.5 MeV and predicts enhanced yields above this energy. GC consistently overstates the data in the studied energy range. PACE predicts amplified cross sections exhibiting a sizable deviation from the data in the low energy region and standing close to the data in the high energy tail of the EF with a slightly shifted trend. As conveyed in Fig. 3(f), the measured data of ^{69}As

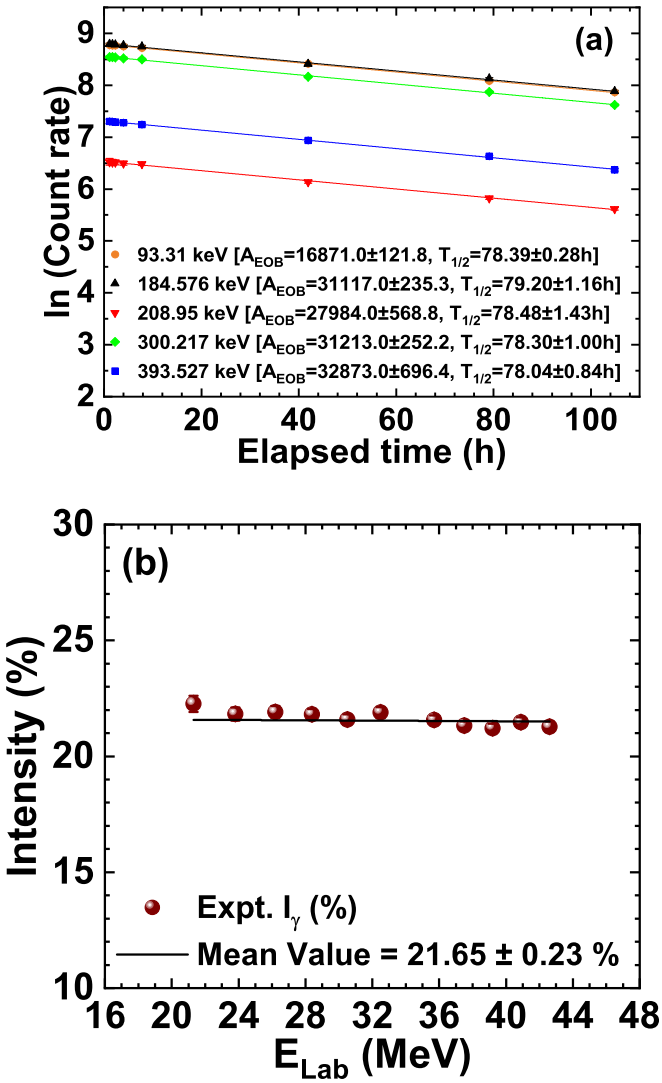

FIG. 2. (a) Experimental decay curves and half-life of ^{67}Ga from distinct γ lines measured in one of the target foil. The slope of a linear fit to the data gives the half-life, and the uncertainty in $T_{1/2}$ is from the systematic error in the linear fit. A_{EOB} has units Bq. (b) The experimental intensity of 93.31 keV γ line was obtained from different target foils. The solid black line denotes the mean value of the intensity. E_{Lab} is the incident energy in the laboratory frame.

residue show close agreement with both EMPIRE EGSM as well as PACE predictions (with a slight deviation of one or two energy points), which predict similar yields within the 24–30 MeV window and diverge significantly above 30 MeV. However, PACE explains the upper limit of the data, while EMPIRE reveals the lower limit of the data at higher energies. GSM reproduces the data within the error bars in the low-energy region, whereas GC does the reverse. As the theory points out, ^{6}Li fusion with ^{64}Zn, ^{66}Zn, ^{67}Zn, and ^{68}Zn isotopes may cause the population of ^{69}As via n, $3n$, $4n$, and $5n$ channels, respectively, with ^{64}Zn and ^{66}Zn contributing significantly. The larger uncertainties associated with ^{69}As data can be accredited to the low production with identification of one or

TABLE III. Comparison of the experimental half-life of ^{67}Ga and its 93.31 keV γ-line intensity with reported values in different databases and Refs. [26,46].

Database	Half-life (h)	E_γ (keV)	I_γ (%)
NuDat3.0 [33]	78.28 ± 0.012	93.31 ± 0.05	38.81 ± 0.03
LUND [41]	78.27 ± 0.014	93.311 ± 0.05	39.2 ± 1.0
NDS [42]	78.28 ± 0.012	93.31 ± 0.05	38.81 ± 0.03
JAEA [43]	78.28 ± 0.012	93.31 ± 0.05	38.81 ± 0.03
KAERI [44]	78.28 ± 0.012	93.31 ± 0.05	38.81 ± 0.03
Singh *et al.* [26]	78.42 ± 0.33	93.31	21.41 ± 0.41
Kumar *et al.* [46]	78.60 ± 1.5	93.31	21.29 ± 0.32
Present work	78.48 ± 0.45	93.31	21.65 ± 0.23

two characteristic γ rays and a quite short half-life of 15.2 min [26].

Based on the comparative analysis, we can comment that EMPIRE with EGSM and PACE4 with $K = 10$ show better predictive capabilities in reproducing the major xn-channel residual cross sections to a fair extent over GSM and GC level densities. This reveals the population of xn-channel residues through the CF mechanism as both the codes predict residual cross sections in the framework of CF dynamics. Thus, we opted for EMPIRE EGSM and PACE4 $K = 10$ as optimum reference level densities for subsequent analysis. Further, on account of the inconsistency (overestimation) exhibited by optimum EMPIRE EGSM calculations in reproducing the lower energy data of ^{70}As, theoretical investigations were performed in terms of the optional input parameters to examine the abnormality, as suggested in Ref. [46]. Obeying the EMPIRE manual, the first step is to check the sensitivity of theoretical calculations with different level densities, which we report in Fig. 3(d). The next element is the examination of the fitting of discrete levels of ^{70}As, performed using the FITLEV option, which suggested that the fitting was good. Last, one can vary the ATILNO parameter to alter the asymptotic value of the level density parameter (the formalism can be found in Ref. [46]), which in turn modifies the densities of levels of a particular residual nuclide (^{70}As) under examination. For instance, altering the ATILNO parameter from 0.8 to 1.2 (within admissible limits), the asymptotic value of the level density parameter varies from 4.1 to 6.2 (default = 5.2) for ^{70}As. Figure 3(e) displays the effect of the ATILNO parameter on optimum EMPIRE EGSM calculations compared with measured data. Notice that the optimum theoretical cross sections are sensitive to the variation of the ATILNO parameter within an energy window of 16–40 MeV, where low values of ATILNO (i.e., 0.8 or 0.9) favor the low energy experimental data (where optimum EMPIRE EGSM calculations exhibit inconsistency) with a slight underestimation at higher energies. In contrast, higher values of ATILNO (1.1 or 1.2) satisfactorily fit the high-energy data with significant overestimation in the low-energy region. Among all, ATILNO = 0.9 may be regarded as optimal as it stands close to the data in lower as well as higher energy regions. These arguments indicate that the internally calculated cross sections of ^{70}As by EMPIRE are sensitive to the external optional input parameter (ATILNO)

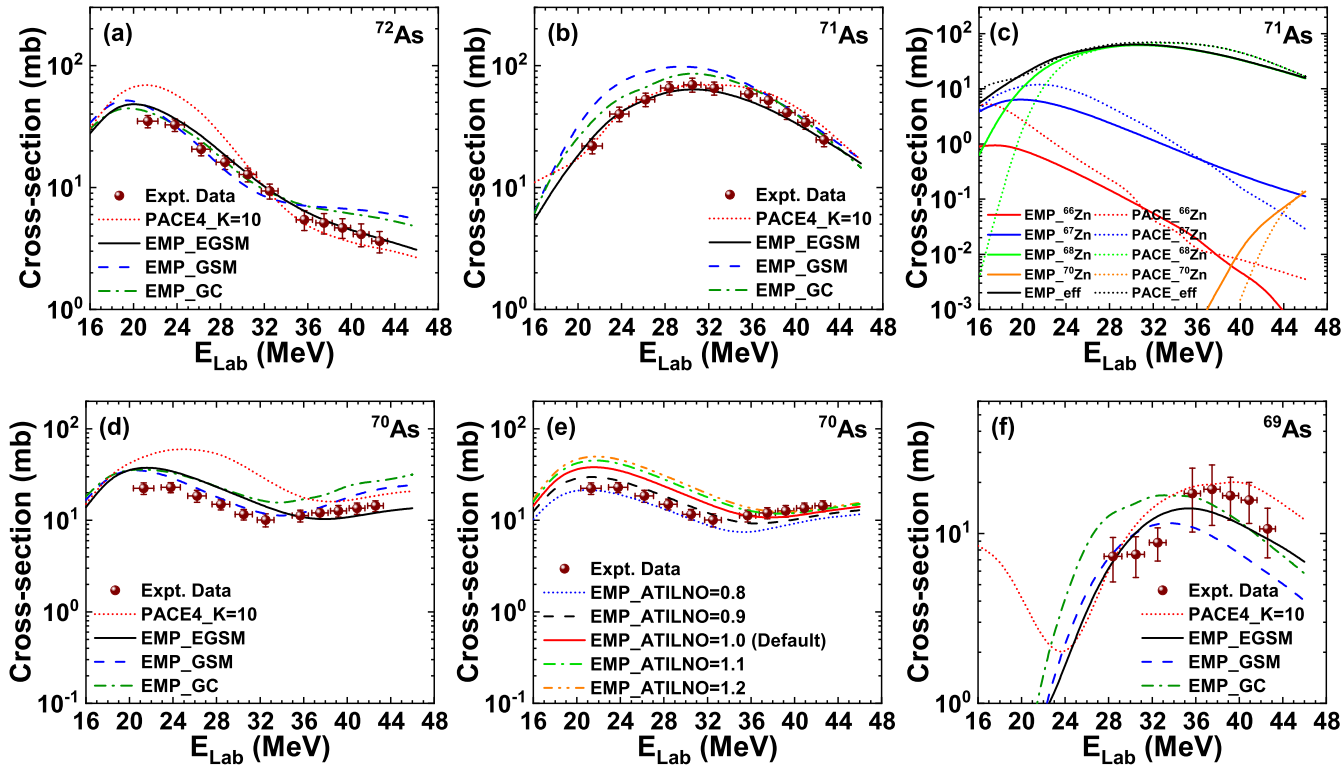

FIG. 3. Comparison of measured EFs (solid dark-red symbols) of residues populated via *xn* channel, viz., (a) ^{72}As, (b) ^{71}As, (d) ^{70}As, and (f) ^{69}As, with theoretical predictions from PACE4 with $K = 10$ (dotted red curve) and EMPIRE3.2.2 with EGSM (solid black curve), GSM (dashed blue curve), and GC (dash-dotted green curve) level densities. Panel (c) projects the abundance-wise contribution from constituent isotopes of Zn in the population of ^{71}As from the ^{6}Li +Zn reaction. Panel (e) displays the effect of the optional ATILNO parameter on EMPIRE EGSM predicted cross sections of ^{70}As in comparison with measured data. Refer to the text for details.

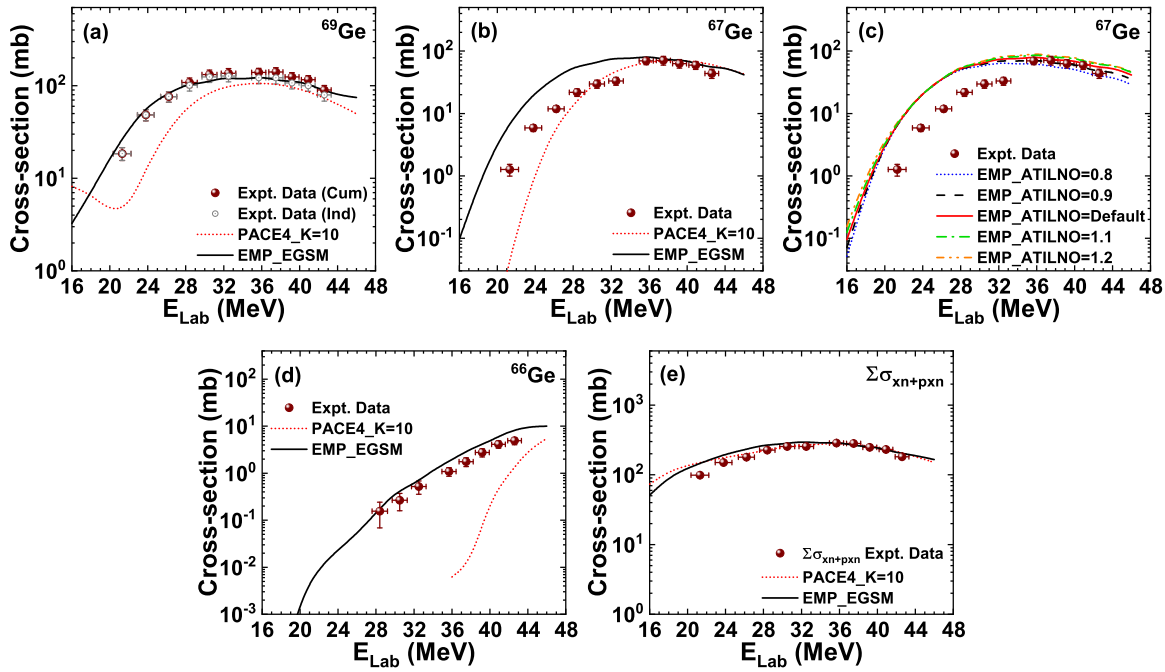

FIG. 4. Comparison of measured EFs of residues populated via *pxn* channel, viz., (a) ^{69}Ge, (b) ^{67}Ge, and (d) ^{66}Ge, with optimal theoretical predictions. The deduced independent cross sections of ^{69}Ge are shown by hollow symbols in panel (a). Panel (c) showcases the effect of the optional ATILNO parameter on the optimum EMPIRE EGSM calculations for ^{67}Ge residue. Panel (e) compares the sum of residual cross sections from *xn* and *pxn* channels (viz., $\Sigma\sigma_{xn+pxn}$) with optimal theoretical references.

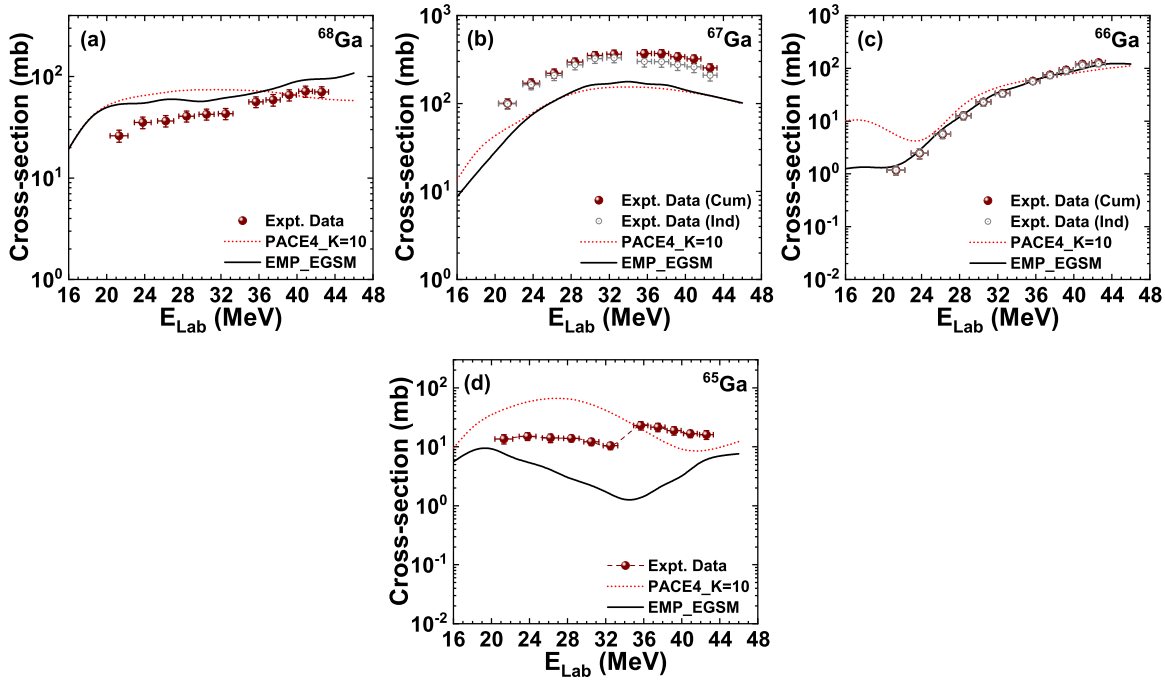

FIG. 5. Same as Fig. 4 but for ^{68,67,66,65}Ga residues populated via αxn channel. The deduced independent cross sections of ^{67,66}Ga residues are shown by hollow symbols. The line joining the measured data of ^{65}Ga portrays the observed trend of EF.

within the energy region of the inconsistency exhibited by optimum (or default ATILNO) calculations. It is worth mentioning that the variation of the ATILNO parameter for a particular residue (^{70}As) does not alter the optimum theoretical cross sections of other residues produced in the reaction.

pxn/αxn *channel.* CN deexcitation through proton channels results in the identification of ^{69,67,66}Ge residues. Figure 4(a) visualizes a comparison of the experimental data of ^{69}Ge residue with optimal theoretical estimations, which was produced cumulatively through *p*, *p*2*n*, *p*3*n*, and *p*4*n* evaporation from the respective CNs formed in ^{6}Li + ^{64,66,67,68}Zn reactions as well as the decay of short-lived precursor ^{69}As. The independent cross sections symbolized by hollow symbols were extracted employing the prescription by Cavinato *et al.* [50]. We observe a good agreement between the independent cross sections of ^{69}Ge residue and EMPIRE EGSM predictions when PACE4 poses an underestimation of data up to 32.5 MeV with an overlap within the uncertainties at higher energies. Portrayed in Fig. 4(b), EGSM calculations overestimate the measured data of ^{67}Ge up to 32.5 MeV and exhibit data agreement beyond it. PACE4 estimates align with the data above 26.2 MeV and undervalue the data below this energy, contrary to EMPIRE yields. The ^{6}Li + ^{64}Zn reaction dominantly populates ^{67}Ge via *p*2*n* or *t* channel with a minimal share from ^{66}Zn (*p*4*n* channel) and ^{67}Zn (*p*5*n* channel) isotopes at higher energies. The overestimation of low energy data of ^{67}Ge by favorable EMPIRE EGSM calculations was further investigated with the variation of optional input ATILNO parameter for ^{67}Ge as reported in Fig. 4(c). EMPIRE EGSM calculations were found to be insensitive to the variation of ATILNO parameter for ^{67}Ge in the energy region of overestimation, though a slight sensitivity can be seen at higher energies within the limit of measured data. The experimental cross sections of ^{66}Ge residue plotted in Fig. 4(d) exhibit compliance with EGSM calculations, in contrast to a complete underestimation by PACE4 predictions. It may be noted that the ^{64}Zn isotope out of ^{nat}Zn plays a dominant role in the production of ^{66}Ge residue via *p*3*n* or tn-channel. Most *pxn*-channel data revealed by EMPIRE EGSM suggest the population of residues via the CF mechanism unambiguously. To assess the aberrant behavior of PACE4 in *p* channels, we plotted the *n*- and *p*-channel cumulative cross sections ($\Sigma\sigma_{xn+pxn}$) in Fig. 4(e), which shows a fair reproduction of $\Sigma\sigma_{xn+pxn}$ data by both the optimum theoretical references [38,51] well in trend. The reproduction of cumulative data by EMPIRE is quite justified as it reasonably reproduces the majority of *n* or *p* channels. It should be noted that the fair justification of $\Sigma\sigma_{xn+pxn}$ data by PACE despite inconsistencies in a few *n* or low energy data of a few *p* channels may be ascribed to the underestimation of low energy insignificant cross sections of *p* channels (where PACE shows disagreement) masked by the overestimation of low energy data of a few *n* channels, thus bringing the cumulative PACE cross sections in close agreement with the measured ones, as given in Refs. [38,51]. Overall, it can be concluded that As (*n* channel) and Ge (*p* channel) residues have cumulatively emerged via the CF mechanism, as no direct processes are anticipated in *n* or *p* channels. Furthermore, the insensitivity of EMPIRE EGSM calculations to the ATILNO parameter on account of inconsistency in the ^{67}Ge case (as reported in literature [10,38–40,49,51–53] for particular *n* or *p* channel residue) poses an open question of the theoretical refinements, as suggested in Ref. [46].

^{68,67,66,65}Ga residues populated via the α-emitting channels were identified from their characteristic γ rays. The experimental EF of ^{68}Ga is compared with the theory in Fig. 5(a), illustrating a thorough overestimation by both the

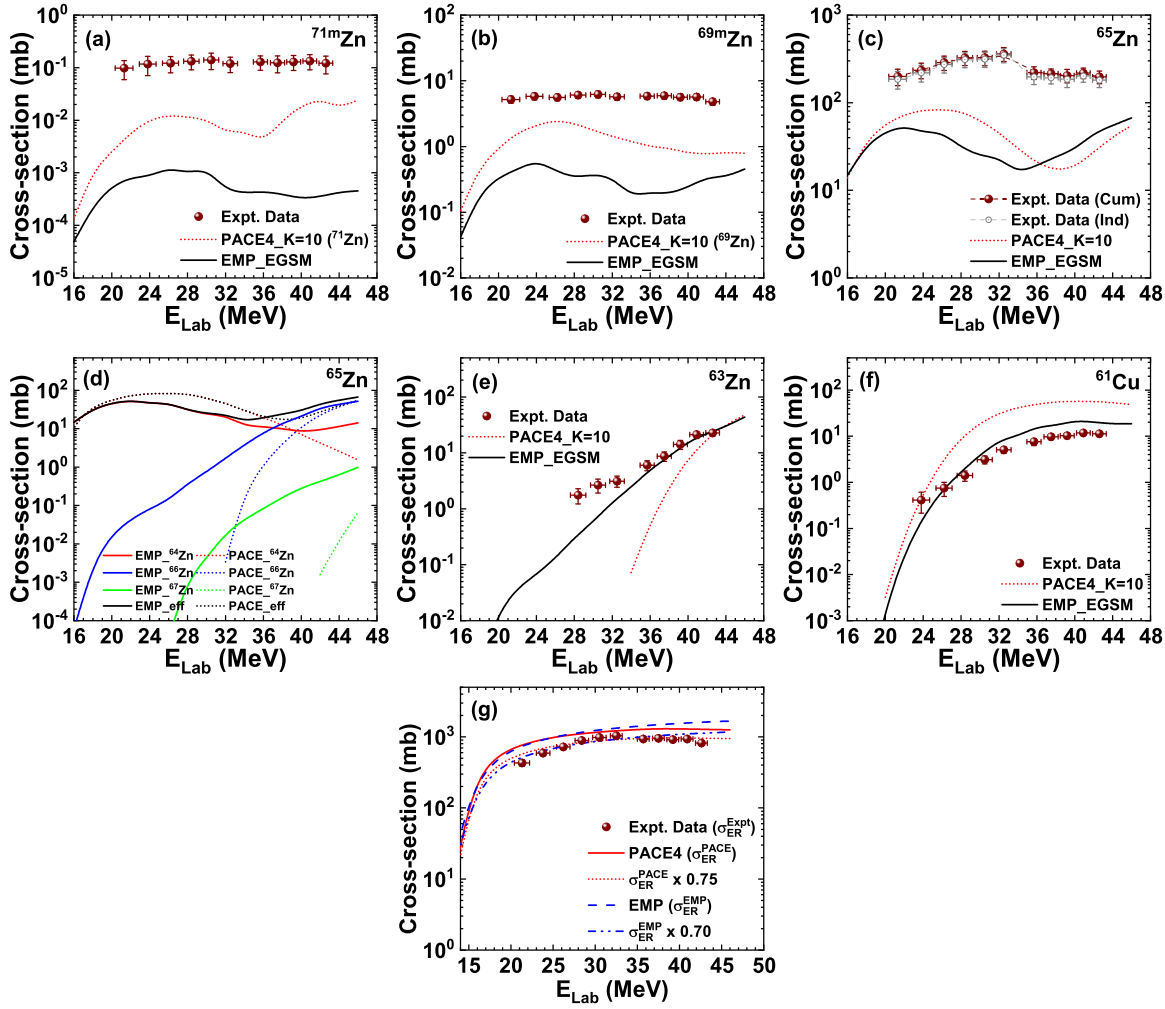

FIG. 6. Same as Fig. 4 but for ^{71m,69m,65,63}Zn and ^{61}Cu residues populated via αpxn and $2\alpha xn$ channels, respectively. Panel (d) displays the contribution of several isotopes in the production of ^{65}Zn. The deduced independent cross sections of ^{65}Zn are shown by hollow symbols. The line joining the measured data of ^{65}Zn portrays the observed trend of EF. Panel (g) compares the measured total residual cross sections (σ_{ER}^{Expt}) with the predicted total residual cross sections by PACE and EMPIRE. Refer to the text for details.

model codes, with PACE4 revealing the data at extreme energies. ^{68}Ga residue may be formed dominantly via $2p$, α, αn, and $\alpha 2n$ channels in ^{6}Li reactions with ^{64}Zn, ^{66}Zn, ^{67}Zn, and ^{68}Zn isotopes, respectively, with a minor contribution from the ^{70}Zn isotope ($\alpha 4n$ channel). Expectedly, due to the cluster structure possessed by the ^{6}Li projectile, almost the same degree of enhancement is witnessed in the ^{67}Ga case relative to the theoretical predictions from both the codes, as presented in Fig. 5(b). The respective compound nuclear deexcitations via $2pn$, αn, $\alpha 2n$, and $\alpha 3n$ channels in ^{6}Li fusion with ^{64}Zn, ^{66}Zn, ^{67}Zn, and ^{68}Zn, respectively, yield the ^{67}Ga residue with a well reproduced trend of EF. The independent cross sections of ^{67}Ga were extracted from the cumulative ones, fed by the deexcitation of the CN and decay of short-lived precursor ^{67}Ge. Figure 5(c) displays the measured EF of ^{66}Ga in accordance with theoretical estimations from both the model codes, where PACE4 exhibits an overestimation of data at two lower energy points. The independent cross sections of ^{66}Ga (populated by the EC decay of short-lived precursor ^{66}Ge as well as the deexcitation of CNs via α, $\alpha 2n$, and $\alpha 3n$-channels in ^{6}Li + ^{64}Zn, ^{66}Zn, and ^{67}Zn reactions, respectively) are shown using hollow symbols. The enhancement in cross section is also observed for ^{65}Ga throughout the energy range compared to EGSM calculations (Fig. 5(d)) and above 32.5 MeV relative to PACE4 predictions. Moreover, PACE4 claims a contrasting behavior of overestimation in low energy regions below 32.5 MeV. ^{6}Li reactions on ^{64}Zn and ^{66}Zn isotopes may result in the formation of ^{65}Ga residue via αn and $\alpha 3n$ channels, respectively. ^{64}Zn contributes significantly in the low energy region and ^{66}Zn at higher energies, justifying the double-humped trend exhibited by the theoretical effective excitation function in line with the measured trend. The observed enhancement in α-emitting channels relative to the theoretical predictions is quite supportive of the low breakup threshold for the ^{6}Li projectile, indicating the existence of a breakup fusion mechanism competing with CF in the population of residues, as reported in earlier studies with WBPs [26,27,38,39,52,53].

$\alpha pxn/2\alpha xn$ channel. Four isotopes of Zn, viz., ^{71m,69m,65,63}Zn, were identified as a consequence of CN

deexcitation through αpxn channels in the ^{6}Li + $^{\text{nat}}$Zn reaction. Figures 6(a) and 6(b) suggest an apparent enhancement in the measured cross sections of ^{71m}Zn and ^{69m}Zn nuclides, respectively, relative to the isomeric cross sections predicted by EMPIRE with EGSM. It should be noted that PACE4 does not estimate the isomeric cross sections disjointly. Thus we show $^{71m+g}$Zn and $^{69m+g}$Zn cross sections predicted by PACE4 to portray the replicated trend of EFs. One may readily judge that ^{71m}Zn residue populates via $3p$ and αp channels in ^{6}Li reactions with ^{68}Zn and ^{70}Zn, respectively, while ^{69m}Zn was formed via $3pn$, αp, and $\alpha p2n$ or αt channels in ^{6}Li reactions with ^{67}Zn, ^{68}Zn, and ^{70}Zn, respectively. CN deexcitation via αp, $\alpha p2n$, and $\alpha p3n$ channels from ^{6}Li + ^{64}Zn, ^{66}Zn, and ^{67}Zn reactions, respectively, in addition to the decay of short-lived higher charge isobar ^{65}Ga, may contribute to the population of ^{65}Zn. Figure 6(d) suggests that the main contribution comes from ^{64}Zn, with ^{66}Zn and ^{67}Zn playing a role at higher energies, thus resulting in a double-peaked trend of measured effective EF in compliance with theoretical ones. The independent cross sections of ^{65}Zn determined out of the cumulative ones as outlined in Fig. 6(c) also exhibit an enhancement relative to both the model predictions in the studied energy domain. PACE4 better matches the shape of the measured EF than EMPIRE with a slightly shifted trend. As conveyed in Fig. 6(e), the underestimation of data resulted from PACE calculations for ^{63}Zn residue. In contrast, EMPIRE gives an underestimation of data at lower energy up to 35.7 MeV and a sound data reproduction above it. The enhancement trend observed in αpxn-channel cross sections endorses the prevalent breakup fusion mechanism causing the formation of residues in addition to the dominant CF mechanism, as reflected in Refs. [26,27,52,53]. Figure 6(f) displays the measured production cross sections of ^{61}Cu residue populated via $2\alpha xn$ channel, in comparison with theory. We notice an overestimation of data by PACE4 over the entire energy range except one point in the low-energy region being predicted well; EMPIRE predictions stand close to data, implying the role of CF mechanism feeding the production of ^{61}Cu residue. It is worthwhile to mention that ^{6}Li + ^{64}Zn reaction merely results in the population of ^{63}Zn and ^{61}Cu residues via $\alpha p2n$ and $2\alpha n$ channels, respectively, as revealed by theoretical estimations.

Even though the two model codes use the HF formalism for CF dynamics, the observed disparity between the predicted residual cross sections could be attributed to their distinct computation approaches and inputs, such as fusion cross section models, empirical transmission coefficients for particle evaporation, and level densities. Furthermore, the role of PEQ in reaction (tested through switching off the PEQ controlling parameter PCROSS in the EM model of EMPIRE code with other parameters unaltered) remains trivial. Thus, the equilibrium process is predominant, with no sign of PEQ. Figure 6(g) compares measured total residual cross sections with total fusion cross sections predicted by the two model codes. It should be noted that we could measure ≈70–75% of fusion data compared to the theoretical predictions by EMPIRE or PACE [Fig. 6(g)]. The observed discrepancy may be accredited to the missing channels (stable or short-lived residues), as suggested in Refs. [26,27,40,49]. The fraction of stable residues from the reaction constitutes ≈22–18% of total fusion cross sections predicted by theory. Moreover, the slight divergence of total fusion predicted by EMPIRE (at higher energies) in comparison with PACE estimates, as shown in Fig. 6(g), may be due to the disparity of predicted residual yields by the two model codes.

C. Justification of the enhanced α-channel cross sections: Signatures of breakup fusion

The results from the EF analysis assert a fundamental role of the CF mechanism in n- and p-emitting channels as the measured $\Sigma\sigma_{xn+pxn}$ data are fairly reproduced by both model codes. A competing alternative mode of fusion (probably breakup fusion) in addition to the dominant CF [54,55] can be interpreted on account of the enhanced residual cross sections in α-emitting channels, owing to the low breakup threshold of the ^{6}Li projectile. The following probable explanations are anticipated because of the substantial residual yields in α-emitting channels, and the discussion has been restricted to the most abundant isotope of Zn (^{64}Zn) to justify the observations. However, there will be a contribution from each abundant isotope of Zn in the population of residues via CF as well as ICF depending on the respective reaction channel thresholds and the excitation energy of the compound nuclei ^{70,72,73,74,76}As* formed in ^{6}Li fusion with ^{64,66,67,68,70}Zn isotopes, respectively. Thus, a similar kind of analysis with other isotopes can be perceived, though we have presented the discussion with most abundant isotope ^{64}Zn for understanding.

(1) The CF mechanism proceeds via the formation of an equilibrated CN through the complete blending of interacting nuclei followed by the emission of ejectiles via different deexcitation channels to form cold residues. Table IV manifests the favored population of residues via CF mechanism as the excitation energy of the CN (for instance, $E^{*} \approx 51.7$ MeV at the highest bombarding energy) formed through this mode is sufficiently higher than the reaction thresholds (Table IV) to populate the residues. The possibility of t emission or other channels from the CN were also considered, in line with theory.

(2) The breakup fusion (ICF) mechanism proceeds via the projectile fragmentation ($\alpha + d$) in the field of the target nucleus due to a low breakup threshold followed by the fusion of either fragment α (or d) with the target, and remnant d (or α) moving as a spectator in the beam direction with proportionate velocity. This process also breeds the identical residues emerging from α channels post-evaporation of ejectiles from the reduced CN, thus, enhancing the residual yields through the breakup fusion mode. Apart from the direct prompt breakup of ^{6}Li, a sequential breakup from 1^{+} and 2^{+} excited inelastic resonant states [6] may also feed the residual yield. The energy of the breakup fragment supports the feasibility of breakup fusion [26]: $E_{\text{frag}} = (E_{\text{in}} - S_{\alpha}) \times (m_{\text{frag}}/m_{\text{in}})$, where E_{in} is the incident energy of the projectile, S_{α} is the α separation energy for ^{6}Li, and m_{frag} and m_{in} are the masses of breakup

TABLE IV. Contributory CF and ICF reaction channels with corresponding reaction thresholds (E_{th}) populating the residues in the ^{6}Li + ^{64}Zn reaction. E_{th} for population of ^{67}Ga through d-ICF channel is mentioned with ^{66}Zn isotope.

		ICF of ^{6}Li (^{6}Li → $\alpha + d$)	
CF of ^{6}Li	E_{th} (MeV)	α-ICF (E_α = 27.7–13.2 MeV)	E_{th} (MeV)
^{64}Zn(^{6}Li, γ)^{70}As	0.0	^{64}Zn(α, p)^{67}Ga	4.2
^{64}Zn(^{6}Li, n)^{69}As	0.0	^{64}Zn(α, t)^{65}Ga	16.7
^{64}Zn(^{6}Li, p)^{69}Ge	0.0	^{64}Zn(α, ^{3}He)^{65}Zn	13.2
^{64}Zn(^{6}Li, t)^{67}Ge	4.5	^{64}Zn(α, αn)^{63}Zn	12.5
^{64}Zn(^{6}Li, tn)^{66}Ge	14.5	d-ICF (E_d = 13.8–6.6 MeV)	E_{th} (MeV)
^{64}Zn(^{6}Li, 2p)^{68}Ga	0.6	^{64}Zn(d, n)^{65}Ga	0.0
^{64}Zn(^{6}Li, 2pn)^{67}Ga	8.4	^{64}Zn(d, p)^{65}Zn	0.0
^{64}Zn(^{6}Li, α)^{66}Ga	0.0	^{64}Zn(d, t)^{63}Zn	5.7
^{64}Zn(^{6}Li, αn)^{65}Ga	0.3	^{66}Zn(d, n)^{67}Ga	0.0
^{64}Zn(^{6}Li, αp)^{65}Zn	4.6		
^{64}Zn(^{6}Li, $\alpha p2n$)^{63}Zn	17.0		
^{64}Zn(^{6}Li, 2αn)^{61}Cu	3.1		

fragment and projectile, respectively. The fragment's energy is adequate to form the reduced CN (with $E^* \approx 29.5$ MeV for α-ICF, 24.3 MeV for d-ICF at highest bombarding energy), which eventually decays to populate the enhancement exhibiting channels, as inferred from the reaction thresholds for ICF channels, shown in Table IV along with contributory reactions. One may notice that the enhancement depicted by Ga and Zn residues is energetically favored via α as well as d capture by the target nucleus. However, as quoted in Refs. [8,56], d capture is more probable over α capture due to lower reaction thresholds.

(3) The transfer-triggered breakup channels may also favor the production of residues as recognized in several in-beam studies [4,5,7]. In this series, 1n-stripping (^{6}Li + ^{64}Zn → ^{65}Zn + ^{5}Li /$\alpha + p$) followed by the prompt breakup of ^{5}Li into $\alpha + p$ constituents [4,5,7] proceeding via fusion of either of these fragments with ^{64}Zn or ^{65}Zn target nuclei may yield the residues. The n-stripping is backed by the positive Q values (+2.3 MeV for ^{5}Li production and +4.3 MeV for $\alpha + p$) of the processes. However, p capture by the target may dominate over α capture, as indicated by the reaction thresholds. The positive Q value (+0.2 MeV) may also favor the p-stripping (^{6}Li + ^{64}Zn → ^{65}Ga + ^{5}He /$\alpha + n$) process [57] with subsequent dissociation of ^{5}He into $\alpha + n$ fragments. The fusion of α or n with the target may lead to residues. However, major inclusive α production (≈50%) was observed by Castaneda *et al.* [58] from ^{6}Li → $\alpha + d$ and ^{6}Li → ^{5}He → $\alpha + n$ exclusive breakups in ^{6}Li + ^{197}Au system. They also suggested an almost equal probability of p- and n-stripping induced breakup processes. d pickup (^{6}Li + ^{64}Zn → ^{62}Cu + ^{8}Be) followed by the breakup of ^{8}Be from excited resonance states like 2^+ into $\alpha + \alpha$ components [4,7,59] may also influence the fusion process owing to the positive Q value (+5.9 MeV) for the process and fulfilled Q value matching condition (i.e., the ground state Q value is comparable to the optimum Q value in the studied energy range). Subsequent fusion of either of these α's with ^{64}Zn or ^{62}Cu target nuclei may thus populate the residues. Furthermore, a significant contribution from the direct breakup was noted by Souza *et al.* [57] in α-d coincidence measurements for the ^{6}Li + ^{59}Co system. In addition to breakup fusion, a feasible direct n-stripping process may contribute to the observed substantial experimental yield of ^{65}Zn residue.

(4) The possibility of other modes, such as the single-step direct cluster transfer (DCT) [46,54,57] process feeding the residual population by virtue of the positive Q values (+9.4 MeV for d-DCT, +1.9 MeV for α-DCT), should not be overlooked. However, the optimum Q values for these processes in the studied energy range nowhere stand close to the ground state Q values (with either isotope of the target), implying a negligible probability of DCT process in this reaction, as discussed in Ref. [39]. If they happen to coexist in a reaction, the nucleus formed through breakup fusion and DCT modes will remain indistinguishable.

Thus, diverse energetically favored breakup routes may cause the population of ^{67,65}Ga, ^{71m,69m,65,63}Zn residues in addition to the dominant CF mode. Though, the explicit disentanglement of these contributions is constrained by the adopted offline γ spectroscopy. For a better insight into the reaction dynamics, one may prefer to estimate the implicit contribution of direct or transfer-induced breakup fusion employing the data reduction method [38,39,52], interpreting their role in residue production. We quantified ICF cross sections from the enhancement depicting channels at each energy point using the relation, $\Sigma\sigma_{ICF} = \Sigma\sigma_{CF+ICF} - \Sigma\sigma_{CF}$, where $\Sigma\sigma_{CF+ICF}$ and $\Sigma\sigma_{CF}$ denote the sum of measured cross sections of the enhancement exhibiting channels and the sum of theoretically predicted cross sections for the same channels, respectively. A comparison of $\Sigma\sigma_{CF+ICF}$ with $\Sigma\sigma_{CF}$ for the ICF channels in reference to PACE4 predictions [shown in Fig. 7(a)] denotes an increasing trend of relative separation, implying that the surging projectile energy fuels the ^{6}Li breakup probability. The deduced $\Sigma\sigma_{ICF}$ are displayed

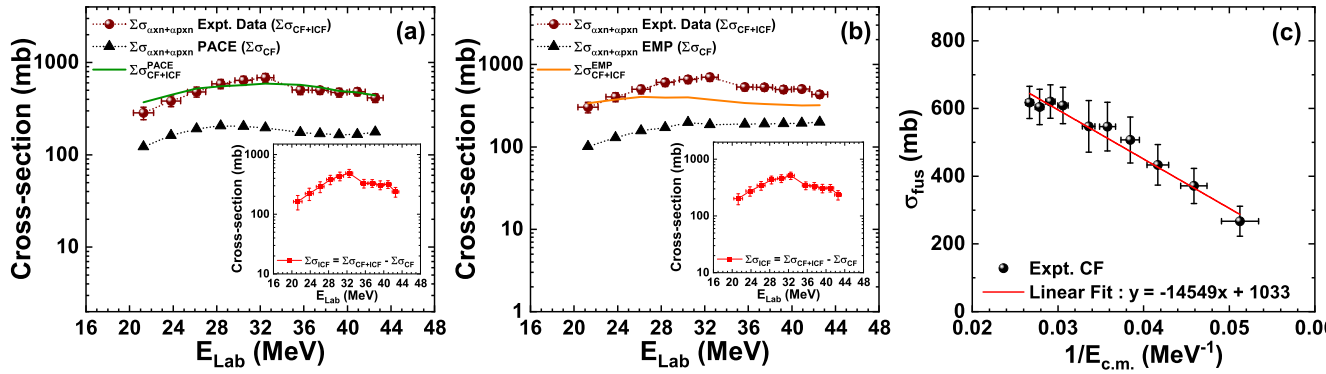

FIG. 7. (a) A comparison of the measured ($\Sigma\sigma_{\mathrm{CF+ICF}}$) and PACE predicted ($\Sigma\sigma_{\mathrm{CF}}$) cross sections as a function of incident energy for the enhancement depicting channels. The solid green line is the empirical fit to the measured $\Sigma\sigma_{\mathrm{CF+ICF}}$ data (refer to the text for details). (b) A similar comparison in context to EMPIRE results for the enhancement depicting respective α channels. The solid orange line is similar empirical curve deduced from EMPIRE predictions. Insets of panels (a) and (b) display the variation of deduced ICF cross sections with bombarding energy in reference to the PACE and EMPIRE codes, respectively. The line joining the data is to guide the eyes. (c) Variation of experimental fusion cross sections (σ_{fus}) as a function of $1/E_{\mathrm{c.m.}}$ for the evaluation of nuclear potential parameters. The solid red line is a linear fit to the data.

in the inset of Fig. 7(a), exhibiting a linear trend with bombarding energy up to 32.5 MeV with a slight deviation from linearity above it, in line with the trend of measured $\Sigma\sigma_{\mathrm{CF+ICF}}$ data from α channels. In order to qualitatively justify the breakup fusion existence, we empirically fitted the measured $\Sigma\sigma_{\mathrm{CF+ICF}}$ data using the relation $\Sigma\sigma^{\mathrm{PACE}}_{\mathrm{CF+ICF}} = \Sigma\sigma_{\mathrm{CF}} + \Sigma(0.75\sigma^{\mathrm{PACE}}_{d\text{-ICF}} + 0.25\sigma^{\mathrm{PACE}}_{\alpha\text{-ICF}})$, where $\Sigma\sigma_{\mathrm{CF}}$ is PACE predicted CF estimate for the enhancement depicting channels as mentioned above, and $\sigma^{\mathrm{PACE}}_{d\text{-ICF}}$ and $\sigma^{\mathrm{PACE}}_{\alpha\text{-ICF}}$ are the PACE predicted d- and α-capture cross sections, respectively, for the same channels computed at corresponding breakup fragment energies (E_{frag}). The resulting empirical curve (solid green line) nicely fits the measured data in Fig. 7(a), which indicates that the discrepancy between the measured $\Sigma\sigma_{\mathrm{CF+ICF}}$ data and theoretical $\Sigma\sigma_{\mathrm{CF}}$ from α channels is due to the unaccounted breakup fusion mechanism in model calculations. Moreover, the empirical ICF contribution $\Sigma(0.75\sigma^{\mathrm{PACE}}_{d\text{-ICF}} + 0.25\sigma^{\mathrm{PACE}}_{\alpha\text{-ICF}})$ also supports the deduced $\Sigma\sigma_{\mathrm{ICF}}$. The empirical relation suggests a dominant contribution from the d capture over α capture in line with published results [8,56]. A similar analysis was also performed with regard to EMPIRE predictions for the enhancement depicting channels as shown in Fig. 7(b), where the empirical curve [solid orange curve in Fig. 7(b)] was deduced from the relation $\Sigma\sigma^{\mathrm{EMP}}_{\mathrm{CF+ICF}} = \Sigma\sigma_{\mathrm{CF}} + \Sigma(0.7\sigma^{\mathrm{EMP}}_{d\text{-ICF}} + 0.3\sigma^{\mathrm{EMP}}_{\alpha\text{-ICF}})$. Symbols denote the same meaning as quoted above in the context of EMPIRE. The empirical curve obtained from EMPIRE predictions fits lower energy points and underestimates the higher energy points by a factor of $\approx$1.4. The empirical $\Sigma\sigma^{\mathrm{EMP}}_{\mathrm{CF+ICF}}$ yields being markedly higher than $\Sigma\sigma_{\mathrm{CF}}$ suggest the breakup fusion contribution. However, the discrepancy between the measured $\Sigma\sigma_{\mathrm{CF+ICF}}$ and empirical curve could be attributed to low d- or α-capture cross sections predicted by EMPIRE compared to PACE4 owing to the obvious reasons mentioned in Sec. IV B. Notably, almost the same orders of $\Sigma\sigma_{\mathrm{ICF}}$ (within errors) were obtained from respective α channels using both model codes, as shown in insets of Figs. 7(a) and 7(b). $\Sigma\sigma_{\mathrm{ICF}}$ is mainly fed by ^{67}Ga and ^{65}Zn residues owing to high experimental yields; also, the use of a natural target might have facilitated the contribution from several contributory channels [26,38,39]. Furthermore, the contribution from breakup fusion in the experimental residual yields of α channels in the present study is supported by the substantial ICF fraction and fusion suppression due to breakup reported in limited studies [9,10,26,38,53,60–65] done with weakly bound or α-clustered particles in the light-medium mass region. Nevertheless, the strength of the breakup fusion mechanism in this mass region remains unclear due to insufficient fusion data, unlike the heavy mass region where segregation of CF and ICF channels is possible because of the restricted population of charged-particle CN deexcitation channels owing to the strong Coulomb field. However, the competing ICF mechanism populates the same channels formed via the dominant CF mechanism in the light-medium mass region. Thus, clear segregation and ambiguities regarding breakup fusion in this mass region should be addressed through a reaction dynamics study using distinct techniques and exploring the dependency on several entrance channel parameters in bulk. The role of entrance channel angular momentum was also judged for the ^{6}Li + ^{64}Zn system in support of the feasibility of breakup fusion. Employing the formalism by Wilczyński *et al.* [23,66], the estimated value of critical angular momentum (ℓ_{crit}) lies in the range [52] 15$\hbar$–22$\hbar$. The maximum angular momentum (ℓ_{max}) for the reaction is found to be less than this range in the studied energy domain, which hints at the contribution of several ℓ bins below ℓ_{crit} (i.e., $\ell < \ell_{\mathrm{crit}}$) in populating the ICF channels. A similar case of the fusion of ℓ boundary was observed in Refs. [16,52,53]. The energy-dependent ℓ_{crit} values [67] lie below ℓ_{max} for most of the energies, suggesting the obvious occurrence of ICF at $\ell > \ell_{\mathrm{crit}}$. A detailed description can be found elsewhere [52].

D. Nuclear potential parameters

The measured fusion data enable an indirect extraction of the potential parameters, such as barrier height and barrier radius, which are difficult to obtain using direct methods.

Theoretically, 1D-BPM-based codes predict the fusion cross sections using the formulation

$$\sigma_{\rm fus}(E_{\rm c.m.}) = \frac{\pi}{k^2}\sum_{\ell=0}^{\infty}(2\ell+1)T_\ell(E_{\rm c.m.}), \quad (1)$$

where T_ℓ is the absorption probability for the ℓth partial wave obtained from the Hill-Wheeler approach; a detailed description can be found elsewhere [27]. The deduced experimental fusion data ($\sigma_{\rm CF} = \sigma_{\rm ER} - \sigma_{\rm ICF}$, where $\sigma_{\rm ER}$ is the sum of all the measured residual cross sections and $\sigma_{\rm ICF}$ is the ICF cross section shown in the inset of Fig. 7(a)) fitted using the Wong's formula [68] [Eq. (2)] under the S-wave approximation yields the fusion barrier:

$$\sigma_{\rm fus}(E_{\rm c.m.}) = \frac{R_B^2\hbar\omega}{2E_{\rm c.m.}}\ln\left\{1+\exp\left[\frac{2\pi}{\hbar\omega}(E_{\rm c.m.}-V_B)\right]\right\}, \quad (2)$$

where R_B, V_B, and $\hbar\omega$ are the barrier radius, height, and curvature, respectively. However, Eq. (2) simplifies to the expression for classical fusion cross section [Eq. (3)] for energies well above the barrier (i.e., $E_{\rm c.m.} - V_B \geqslant \frac{2\pi}{\hbar\omega}$), which follows a linear dependence of $\sigma_{\rm fus}$ on $1/E_{\rm c.m.}$ as shown in Fig. 7(c) for the studied reaction. The inconsistency of Wong's formula for lighter systems at much higher energies [69] has led us to omit a higher energy point to obtain the best linear fit to the data [27].

$$\sigma_{\rm fus}(E_{\rm c.m.}) = \pi R_B^2\left(1-\frac{V_B}{E_{\rm c.m.}}\right). \quad (3)$$

The extracted barrier height and radius are 14.0 ± 0.9 MeV and 5.8 ± 0.2 fm, respectively, with uncertainties from the data fitting. The extracted parameters may be regarded as effective values obtained from the fusion data of the ^{6}Li +$^{\rm nat}$Zn reaction. The values are within acceptable deviation limits reported in the literature (with natural or enriched targets) [27,40,49,70,71] when compared to the values from systematics [72] ranging $V_B = 13.3$–13.6 MeV, $R_B = 8.8$–8.9 fm for the ^{6}Li interaction with individual isotopes of Zn. The slight deviation from systematic values can be ascribed to the unaccounted missing channels constrained by the present measurement technique. This fact is further strengthened by the deduced values of $V_B = 13.4 \pm 0.1$ MeV and $R_B = 8.8 \pm 0.02$ fm from the fitting of theoretical total fusion cross sections (sum of all the residual cross sections predicted by theory, which includes the measured as well as missing channels), lying close to the systematic values as suggested in Ref. [40].

E. Yield of ^{67}Ga: Application radionuclide

Physicochemical properties exhibited by the ^{67}Ga radionuclide make it a potential candidate in nuclear medicine. ^{67}Ga functions well in single-photon emission computed tomography (SPECT) and therapeutic studies for its low-energy high-intensity γ rays [93.31 keV (38.81%), 184.57 keV (21.41%)] and Auger electron emission tendency, respectively [24]. The present study suggests a no-carrier-added (NCA) production of 100.3 ± 13.3–370.3 ± 38.5 mb for ^{67}Ga corresponding to the integral yield of 789.7 MBq/C for a 30.8 mg/cm^2 thick target within the studied energy domain,

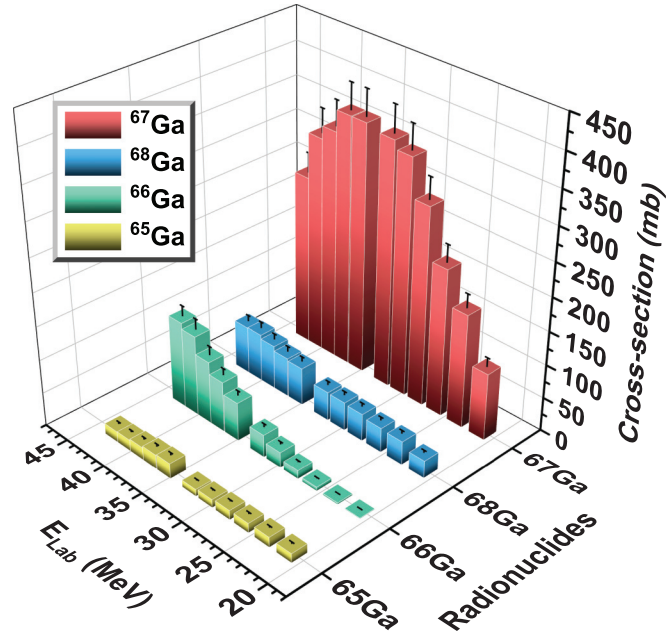

FIG. 8. Comparison of the measured production cross sections of Ga residues.

with a maximum of 370.3 ± 38.5 mb achieved at 37.5 MeV that is promising for clinical purposes. Figure 8 compares the measured cross sections of ^{67}Ga with the isotopic impurities to portray the energy window (21–43 MeV) of clean production. It is pertinent to mention that the longer half-life of ^{67}Ga (3.2617 d) among the coproduced isotopic impurities will favor its contamination-free production, leading to the extraction of pure ^{67}Ga from the target bulk as the nonisotopic impurities can be easily separated chemically.

V. CONCLUSION

For the first time, we put forth the EF analysis of residues populated in the ^{6}Li +Zn reaction within the 21–43 MeV energy range. The experimental EFs were compared with theoretical predictions from PACE4 and EMPIRE3.2.2 model codes to interpret the underlying reaction mechanisms. The analysis reveals a fair reproduction of *xn* and *pxn* channel data ($\Sigma\sigma_{xn+pxn}$) with both the model codes, while a significant enhancement was witnessed in α-emitting channels relative to the theory. Owing to the low breakup threshold of the ^{6}Li projectile, the enhancement was implicitly interpreted as the signatures of direct or transfer-triggered breakup fusion processes in addition to the dominant CF mechanism playing a vital role in the reaction. Nuclear potential parameters extracted from the measured fusion data were reported in proximity to the systematic values, validating the present measurement. We reported a new experimental intensity for the 93.31 keV γ-line from ^{67}Ga decay, which happens to be $21.65 \pm 0.23\%$. Thus, it necessitates the formal intensity measurement through a dedicated experiment to address the ambiguity. Also, the optimized production of medically relevant ^{67}Ga residue and the energy window of NCA production were discussed from the application perspective.

ACKNOWLEDGMENTS

The authors thank the BARC-TIFR Pelletron facility team for their assistance in target preparation and experiment accomplishment. The cooperation and teamwork from TASISPEC Lab, IIT Roorkee, India, is commendable. Research Grant No. CRG/2018/002354 from SERB(IN) and the support of a fellowship from MHRD, Govt. of India, are gratefully acknowledged. We also acknowledge the support of the Department of Atomic Energy, Govt. of India, under Project No. 12P-R&D-TFR-5.02-0300.

[1] V. Jha, V. V. Parkar, and S. Kailas, Phys. Rep. **845**, 1 (2020).
[2] K. Siwek-Wilczyńska, E. H. du Marchie van Voorthuysen, J. van Popta, R. H. Siemssen, and J. Wilczyński, Phys. Rev. Lett. **42**, 1599 (1979).
[3] M. K. Sharma, P. P. Singh, D. P. Singh, A. Yadav, V. R. Sharma, I. Bala, R. Kumar, Unnati, B. P. Singh, and R. Prasad, Phys. Rev. C **91**, 014603 (2015).
[4] D. H. Luong, M. Dasgupta, D. J. Hinde, R. du Rietz, R. Rafiei, C. J. Lin, M. Evers, and A. Diaz-Torres, Phys. Lett. B **695**, 105 (2011).
[5] S. Santra, V. V. Parkar, K. Ramachandran, U. K. Pal, A. Shrivastava, B. J. Roy, B. K. Nayak, A. Chatterjee, R. K. Choudhury, and S. Kailas, Phys. Lett. B **677**, 139 (2009).
[6] A. G. Camacho, A. Diaz-Torres, and H. Q. Zhang, Phys. Rev. C **99**, 054615 (2019).
[7] D. Chattopadhyay, S. Santra, A. Pal, A. Kundu, K. Ramachandran, R. Tripathi, D. Sarkar, S. Sodaye, B. K. Nayak, A. Saxena *et al.*, Phys. Rev. C **94**, 061602(R) (2016).
[8] S. Santra, S. Kailas, V. V. Parkar, K. Ramachandran, V. Jha, A. Chatterjee, P. K. Rath, and A. Parihari, Phys. Rev. C **85**, 014612 (2012).
[9] H. Kumawat, V. Jha, V. V. Parkar, B. J. Roy, S. K. Pandit, R. Palit, P. K. Rath, C. S. Palshetkar, S. K. Sharma, S. Thakur *et al.*, Phys. Rev. C **86**, 024607 (2012).
[10] S. P. Hu, G. L. Zhang, J. C. Yang, H. Q. Zhang, P. R. S. Gomes, J. Lubian, X. G. Wu, J. Zhong, C. Y. He, Y. Zheng *et al.*, Phys. Rev. C **91**, 044619 (2015).
[11] M. Dasgupta, P. R. S. Gomes, D. J. Hinde, S. B. Moraes, R. M. Anjos, A. C. Berriman, R. D. Butt, N. Carlin, J. Lubian, C. R. Morton *et al.*, Phys. Rev. C **70**, 024606 (2004).
[12] L. R. Gasques, D. J. Hinde, M. Dasgupta, A. Mukherjee, and R. G. Thomas, Phys. Rev. C **79**, 034605 (2009).
[13] P. K. Rath, S. Santra, N. L. Singh, R. Tripathi, V. V. Parkar, B. K. Nayak, K. Mahata, R. Palit, S. Kumar, S. Mukherjee *et al.*, Phys. Rev. C **79**, 051601(R) (2009).
[14] S. Kalkal, S. Mandal, N. Madhavan, E. Prasad, S. Verma, A. Jhingan, R. Sandal, S. Nath, J. Gehlot, B. R. Behera *et al.*, Phys. Rev. C **81**, 044610 (2010).
[15] M. Shuaib, V. R. Sharma, A. Yadav, P. P. Singh, M. K. Sharma, D. P. Singh, R. Kumar, R. P. Singh, S. Muralithar, B. P. Singh, and R. Prasad, Phys. Rev. C **94**, 014613 (2016).
[16] H. Kumar, S. A. Tali, M. A. Ansari, D. Singh, R. Ali, A. Ali, S. Parashari, P. K. Giri, S. B. Linda, R. Kumar *et al.*, Phys. Rev. C **99**, 034610 (2019).
[17] P. K. Giri, D. Singh, A. Mahato, S. B. Linda, H. Kumar, S. A. Tali, S. Parasari, A. Ali, M. A. Ansari, R. Dubey *et al.*, Phys. Rev. C **100**, 024621 (2019).
[18] P. R. S. Gomes, R. Linares, J. Lubian, C. C. Lopes, E. N. Cardozo, B. H. F. Pereira, and I. Padron, Phys. Rev. C **84**, 014615 (2011).
[19] R. Rafiei, R. du Rietz, D. H. Luong, D. J. Hinde, M. Dasgupta, M. Evers, and A. Diaz-Torres, Phys. Rev. C **81**, 024601 (2010).
[20] W. Trautmann, Ole Hansen, H. Tricoire, W. Hering, R. Ritzka, and W. Trombik, Phys. Rev. Lett. **53**, 1630 (1984).
[21] C. Gerschel, Nucl. Phys. A **387**, 297 (1982).
[22] H. Utsunomiya, T. Nomura, M. Ishihara, T. Sugitate, K. Ieki, and S. Kohmoto, Phys. Lett. B **105**, 135 (1981).
[23] J. Wilczyński, K. Siwek-Wilczyńska, J. van Driel, S. Gonggrijp, D. C. J. M. Hageman, R. V. F. Janssens, J. Łukasiak, and R. H. Siemssen, Phys. Rev. Lett. **45**, 606 (1980).
[24] S. M. Qaim, Nucl. Med. Biol. **44**, 31 (2017).
[25] J. F. Ziegler, M. D. Ziegler, and J. P. Biersack, Nucl. Instrum. Methods Phys. Res., Sect. B **268**, 1818 (2010).
[26] A. Singh, M. Maiti, T. N. Nag, and S. Sodaye, Phys. Scr. **98**, 025306 (2023).
[27] R. Prajapat and M. Maiti, Phys. Rev. C **101**, 024608 (2020).
[28] A. Gavron, Phys. Rev. C **21**, 230 (1980).
[29] M. Herman, R. Capote, B. V. Carlson, P. Oblozinsky, M. Sin, A. Trkov, H. Wienke, and V. Zerkin, Nucl. Data Sheets **108**, 2655 (2007).
[30] W. Hauser and H. Feshbach, Phys. Rev. **87**, 366 (1952).
[31] R. Bass, Phys. Rev. Lett. **39**, 265 (1977).
[32] D. L. Hill and J. A. Wheeler, Phys. Rev. **89**, 1102 (1953).
[33] National Nuclear Data Center, Brookhaven National Laboratory, https://www.nndc.bnl.gov/nudat3/.
[34] R. Capote, M. Herman, P. Obložinský, P. G. Young, S. Goriely, T. Belgya, A. V. Ignatyuk, A. J. Koning, S. Hilaire, V. A. Plujko *et al.*, Nucl. Data Sheets **110**, 3107 (2009).
[35] A. Gilbert and A. G. W. Cameron, Can. J. Phys. **43**, 1446 (1965).
[36] A. V. Ignatyuk, J. L. Weil, S. Raman, and S. Kahane, Phys. Rev. C **47**, 1504 (1993).
[37] A. D'Arrigo, G. Giardina, M. Herman, A. V. Ignatyuk, and A. Taccone, J. Phys. G: Nucl. Part. Phys. **20**, 365 (1994).
[38] D. Kumar, M. Maiti, and S. Lahiri, Phys. Rev. C **96**, 014617 (2017).
[39] R. Prajapat and M. Maiti, Phys. Rev. C **101**, 064620 (2020).
[40] M. Sagwal and M. Maiti, Phys. Rev. C **107**, 034609 (2023).
[41] S. Y. F. Chu, L. P. Ekström, and R. B. Firestone, WWW Table of Radioactive Isotopes, The Lund/LBNL Nuclear Data Search, 1999, http://nucleardata.nuclear.lu.se/toi/.
[42] Live Chart of Nuclides: Nuclear Structure and Decay Data, NDS, IAEA, 2019, https://www-nds.iaea.org/relnsd/vcharthtml/VChartHTML.html.
[43] WWW Chart of the Nuclides, Japanese Nuclear Data Library, 2014, https://wwwndc.jaea.go.jp/CN14/index.html.
[44] Table of γ-rays, Nuclear Data Center, Korean Atomic Energy Research Institute (KAERI), 2015, http://atom.kaeri.re.kr/.
[45] B. M. Ali, G. Y. Mohamed, F. Ditrói, S. Takács, and M. Al-Abyad, Phys. Rev. C **102**, 064608 (2020).
[46] R. Kumar, M. Maiti, T. N. Nag, and S. Sodaye, Phys. Rev. C **104**, 064606 (2021).
[47] E. Nigron, A. Guertin, F. Haddad, and T. Sounalet, Front. Med. **8**, 674617 (2021).

[48] G. Pupillo, L. Mou, P. Martini, M. Pasquali, A. Boschi, G. Cicoria, A. Duatti, F. Haddad, and J. Esposito, Radiochim. Acta **108**, 593 (2020).
[49] R. Kumar, M. Maiti, G. Sarkar, M. Sagwal, P. Kaur, R. Prajapat, T. N. Nag, and S. Sodaye, Eur. Phys. J. A **57**, 209 (2021).
[50] M. Cavinato, E. Fabrici, E. Gadioli, E. Gadioli Erba, P. Vergani, M. Crippa, G. Colombo, I. Redaelli, and M. Ripamonti, Phys. Rev. C **52**, 2577 (1995).
[51] R. Prajapat, M. Maiti, and D. Kumar, Phys. Rev. C **103**, 014608 (2021).
[52] R. Prajapat and M. Maiti, Phys. Rev. C **103**, 034620 (2021).
[53] A. Singh and M. Maiti, Phys. Rev. C **107**, 054610 (2023).
[54] A. Di Pietro, P. Figuera, E. Strano, M. Fisichella, O. Goryunov, M. Lattuada, C. Maiolino, C. Marchetta, M. Milin, A. Musumarra *et al.*, Phys. Rev. C **87**, 064614 (2013).
[55] P. R. S. Gomes, M. D. Rodríguez, G. V. Martí, I. Padron, L. C. Chamon, J. O. Fernández Niello, O. A. Capurro, A. J. Pacheco, J. E. Testoni, A. Arazi, M. Ramirez, R. M. Anjos, J. Lubian, R. Veiga, R. Liguori Neto, E. Crema, N. Added, C. Tenreiro, and M. S. Hussein, Phys. Rev. C **71**, 034608 (2005).
[56] V. V. Parkar, S. K. Pandit, A. Shrivastava, R. Palit, K. Mahata, V. Jha, K. Ramachandran, S. Gupta, S. Santra, S. K. Sharma *et al.*, Phys. Rev. C **98**, 014601 (2018).
[57] F. A. Souza, C. Beck, N. Carlin, N. Keeley, R. L. Neto, M. M. de Moura, M. G. Munhoz, M. G. Del Santo, A. A. P. Suaide, E. M. Szanto *et al.*, Nucl. Phys. A **821**, 36 (2009).
[58] C. M. Castaneda, H. A. Smith, Jr., P. P. Singh, and H. Karwowski, Phys. Rev. C **21**, 179 (1980).
[59] K. J. Cook, E. C. Simpson, D. H. Luong, S. Kalkal, M. Dasgupta, and D. J. Hinde, Phys. Rev. C **93**, 064604 (2016).
[60] A. Agarwal, A. K. Jashwal, M. Kumar, S. Prajapati, S. Dutt, M. Gull, I. A. Rizvi, K. Kumar, S. Ali, A. Yadav *et al.*, Phys. Rev. C **103**, 034602 (2021).
[61] R. Ali, D. Singh, M. A. Ansari, M. H. Rashid, R. Guin, and S. K. Das, J. Phys. G: Nucl. Part. Phys. **37**, 115101 (2010).
[62] F. K. Amanuel, B. Zelalem, A. K. Chaubey, A. Agarwal, I. A. Rizvi, A. Maheshwari, and T. Ahmed, Phys. Rev. C **84**, 024614 (2011); Eur. Phys. J. A **47**, 156 (2011).
[63] S. Ali, T. Ahmad, K. Kumar, I. A. Rizvi, A. Agarwal, S. S. Ghugre, A. K. Sinha, and A. K. Chaubey, J. Mod. Phys. **05**, 2063 (2014).
[64] D. Singh, R. Ali, M. Afzal Ansari, B. S. Tomar, M. H. Rashid, R. Guin, and S. K. Das, Phys. Rev. C **83**, 054604 (2011).
[65] M. F. Guo, G. L. Zhang, P. R. S. Gomes, J. Lubian, and E. Ferioli, Phys. Rev. C **94**, 044605 (2016).
[66] J. Wilczyński, Nucl. Phys. A **216**, 386 (1973).
[67] M. V. Chushnyakova and I. I. Gontchar, Nucl. Phys. A **941**, 255 (2015).
[68] C. Y. Wong, Phys. Rev. Lett. **31**, 766 (1973).
[69] N. W. Lwin, N. N. Htike, and K. Hagino, Phys. Rev. C **95**, 064601 (2017).
[70] R. Prajapat, M. Maiti, R. Kumar, M. Sagwal, Gonika, C. Kumar, R. Biswas, J. Gehlot, S. Nath, and N. Madhavan, Phys. Rev. C **105**, 064612 (2022).
[71] W. Scobel, H. H. Gutbrod, M. Blann, and A. Mignerey, Phys. Rev. C **14**, 1808 (1976).
[72] http://nrv.jinr.ru/nrv/webnrv/qcalc/.